

Novel Magnetic Ni-N-Ni Centers in N-substituted NiO

Simon Godin,^{1,2,*} Ilya S. Elfimov,^{1,2} Fengmiao Li,^{1,2} Bruce A. Davidson,^{1,2} Ronny Sutarto,³ Jonathan D. Denlinger,⁴ Liu Hao Tjeng,⁵ George A. Sawatzky,^{1,2} and Ke Zou^{1,2}

¹*Department of Physics and Astronomy, University of British Columbia, Vancouver, British Columbia V6T 1Z4, Canada*

²*Quantum Matter Institute, University of British Columbia, Vancouver, British Columbia V6T 1Z4, Canada*

³*Canadian Light Source, Saskatoon, Saskatchewan S7N 2V3, Canada*

⁴*Advanced Light Source, Lawrence Berkeley National Laboratory, Berkeley, CA 94720, USA*

⁵*Max Planck Institute for Chemical Physics of Solids, Nöthnitzer Straße 40, 01187 Dresden, Germany*

(Dated: December 31, 2024)

Following the concept of creating individual centers, we investigate local electronic states and magnetic ordering in nickel oxide (NiO) induced by substituting oxygen (O) with nitrogen (N). Each N introduces an additional N 2p hole and alters the state of the magnetic moment at a neighboring nickel (Ni) cation site, as the exchange interaction between this hole and the Ni e_g electrons dominates the superexchange interaction. This leads to the formation of Ni-N-Ni units consisting of five spins that are decoupled from the rest of the antiferromagnetic (AFM) NiO lattice and exhibit degenerate spin states. These centers are studied using density functional theory and confirmed through high-resolution spectroscopy measurements on N-substituted NiO thin films grown by molecular beam epitaxy. This type of magnetic design could potentially advance quantum technologies based on strongly correlated materials, such as quantum sensors and spin-qubits.

The doping of transition metal oxides has been a broad area of study with significant fundamental interest and numerous practical applications. Nickel monoxide (NiO) in particular is an intriguing material, often regarded as an exemplary strongly correlated system. NiO is a charge-transfer insulator with a 4 eV bandgap, located in the intermediate regime of the Zaanen-Sawatzky-Allen scheme[1], exhibiting strong hybridization between Ni 3d and O 2p. It has an antiferromagnetic (AFM) rock-salt structure with a lattice parameter $a = 4.176 \text{ \AA}$, a Néel temperature (T_N) of 523 K, and a magnetic moment of $2 \mu_B$ at each Ni site in its bulk stoichiometric form. The AFM superexchange coupling of the Ni next nearest-neighbors leads to ferromagnetic (FM) (111) planes, as well as a complex set of possible domain walls and spin domains at the surface[2, 3]. The replacement of Ni cations with other 3d transition metals, such as manganese (Mn) and cobalt (Co), which varies the number of 3d electrons, has been shown to significantly impact magnetic properties[4, 5]. What remains intriguing, yet still lacks rigorous investigation, is the effect of anion substitution in NiO, such as nitrogen (N). It is expected to significantly alter local electronic and magnetic interactions, considering the more extensive 2p orbital and the one less electron in N compared to O.

Anion substitution using N and carbon (C) in various materials has found use in the fields of photonics and quantum information. Key among them are quantum sensors, the most common being nitrogen-vacancy (NV) centers, consisting of a neighboring C vacancy and an N-substituted C site in diamond. They enable the detection of single electron and nuclear spins in nanoscale-resolution scanning microscopy and also serve as spin qubits[6–8]. Efforts are ongoing to extend the use of spin centers to other materials, such as defects in sili-

con (Si)[9, 10], hexagonal boron nitride (hBN) [11], and SiC[12].

In this letter, we demonstrate experimentally that incorporating low concentrations of N in NiO thin films induces in-gap states of N 2p character. The substitution of an O with N flips the spin of a neighboring Ni, forming a Ni-N-Ni unit decoupled from the AFM lattice, with total spin $S = 3/2$ and two degenerate states: $(\uparrow\uparrow - \downarrow\downarrow - \uparrow\uparrow)$ and $(\downarrow\downarrow - \uparrow\uparrow - \downarrow\downarrow)$. The absence of coupling to the lattice results in degenerate states ($m_s = -3/2, -1/2, 1/2, 3/2$), which could be split by an external magnetic field.

We validate these results through both density functional theory (DFT) calculations and spectroscopy experiments on $\text{NiO}_{1-x}\text{N}_x$ thin films grown by molecular beam epitaxy (MBE). Using experimental and calculated X-ray absorption spectroscopy (XAS), we provide direct evidence of a change in the magnetic property of Ni, as well as the presence of N impurity states in the bandgap. We also observe the emergence of states below the Fermi energy using angle-resolved photoemission spectroscopy (ARPES) and confirm the N character of the introduced holes through X-ray photoelectron spectroscopy (XPS). Anion-substituted NiO prepared using MBE is stable in air, and can be handled *ex situ*, making it an attractive candidate for practical applications.

Figure 1 shows DFT+U calculations of N-substituted NiO (see Supplementary Material [13] for additional details on the calculation methods). The electron's on-site effective interactions for the Ni 3d, O 2p, and N 2p states are $U = 6 \text{ eV}$, 4 eV , and 3 eV , respectively. The substitution of O atoms with N in NiO leads to hole doping, introducing one hole per N. Our calculations indicate that these holes primarily exhibit N 2p character and that the oxidation state of the Ni atoms remains unaffected, i.e.

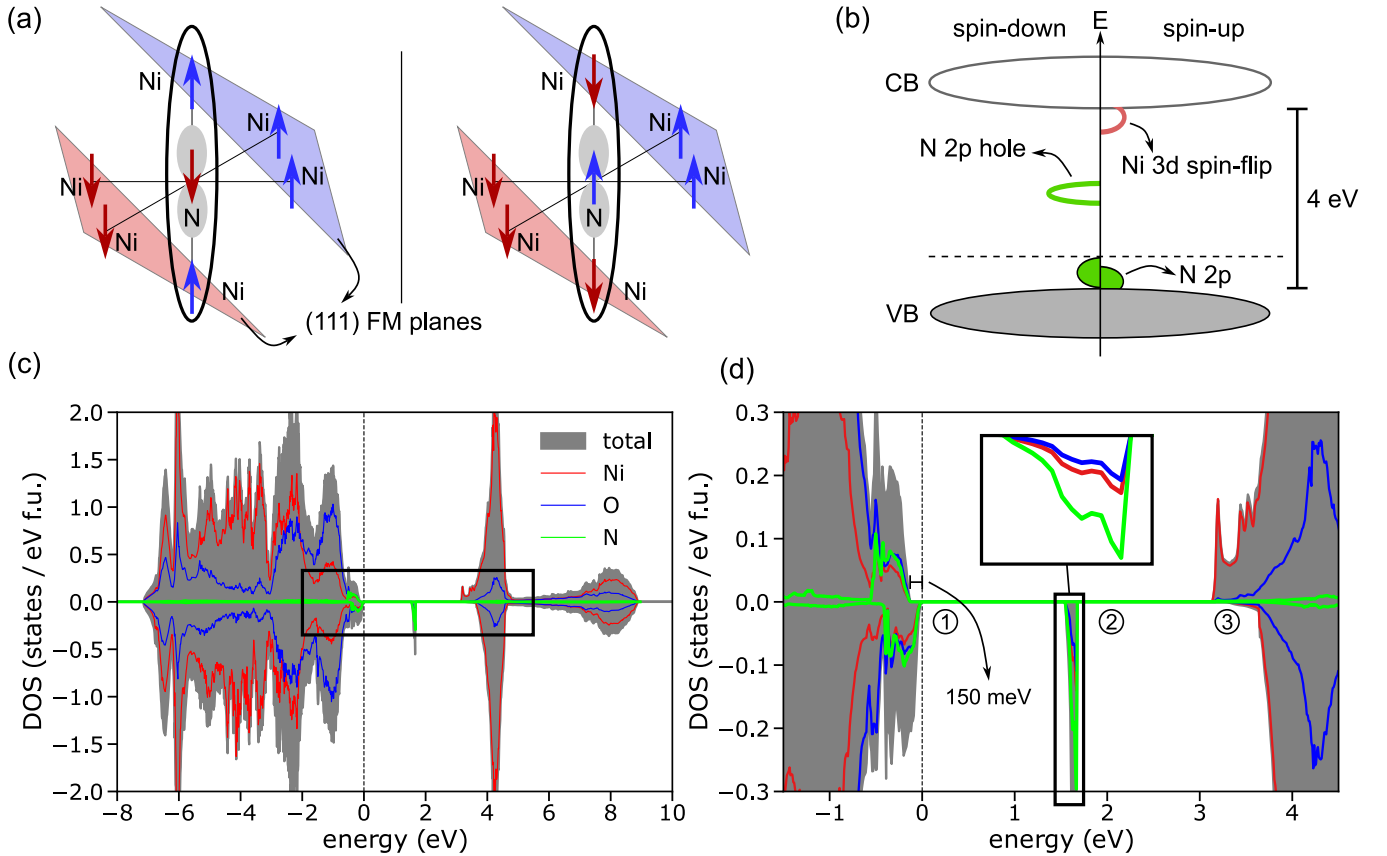


FIG. 1. Density functional theory (DFT) calculations of N-substituted NiO, with one out of thirty-two O atoms replaced by an N. (a) Representation of the Ni-N-Ni unit. The presence of the N flips the spin of a neighboring Ni within its (111) FM plane. The states with an N 2p hole aligned spin-down (or spin-up) and both Ni 3d aligned spin-up (or spin-down) are degenerate. (b) Schematics of the introduced PDoS near the bandgap of NiO upon N substitution. (c) PDoS of Ni, O, and N resulting from this configuration. (d) Zoom on the energy window around the bandgap of $\text{NiO}_{1-x}\text{N}_x$ showing N, Ni, and O's PDoS. The labels (1), (2), and (3) point to the shoulder to the valence band, impurity states, and shoulder to the conduction band, respectively. These features are shown in (b). The zero of energy represents the Fermi energy.

Ni^{2+} . The arrangement in which each N atom flips the spin of a neighboring Ni atom within its FM plane [see Fig. 1(a)] significantly lowers the energy of the system by 204 meV, indicating that the spin-flipped configuration is very stable. Notably, the rest of the AFM order and overall structure are preserved throughout the rest of the material.

Figure 1(b) schematically shows the main features of the resulting spin-resolved partial density of states (PDoS) that depart from unsubstituted NiO. It shows how an N 2p hole forms spin-polarized impurity states within the bandgap. This configuration also affects the states of the associated spin-flipped Ni, forming a shoulder below the conduction band (with opposite spin than the one of the N 2p hole). Additionally, spin-polarized states appear above the valence band.

Figure 1(c) shows the computed PDoS results in N-substituted NiO, in the configuration where a Ni is flipped to spin-up and the N is spin-down, as described above. Figure 1(d) is a zoom of (c), around the region

of interest. At the top of the valence band (1), the spin-down states are shifted compared to spin-up by approximately 150 meV, from the strong direct exchange between the N 2p and both surrounding Ni 3d. It is important to note that this is almost one order of magnitude stronger than the superexchange interaction of around 20 meV between the Ni 3d through the full O 2p orbitals in NiO[14–16]. We can also observe the impurity states (2), dominated by N 2p and the shoulder to the conduction band (3). Additional PDoS results for other arrangements can be found in Supplementary Material[13]. We show the case of Ni spin-flipped unsubstituted NiO, where flipping the spin of one Ni costs 117 meV, confirming that anion substitution is required for this effect to be advantageous. We further show the energetically unfavorable ground state of $\text{NiO}_{1-x}\text{N}_x$ with no Ni spin-flip.

In unsubstituted NiO, the AFM superexchange interaction between Ni atoms, mediated by an O atom, results in two triangular arrangements of Ni spins in an AFM configuration. The large exchange interaction between

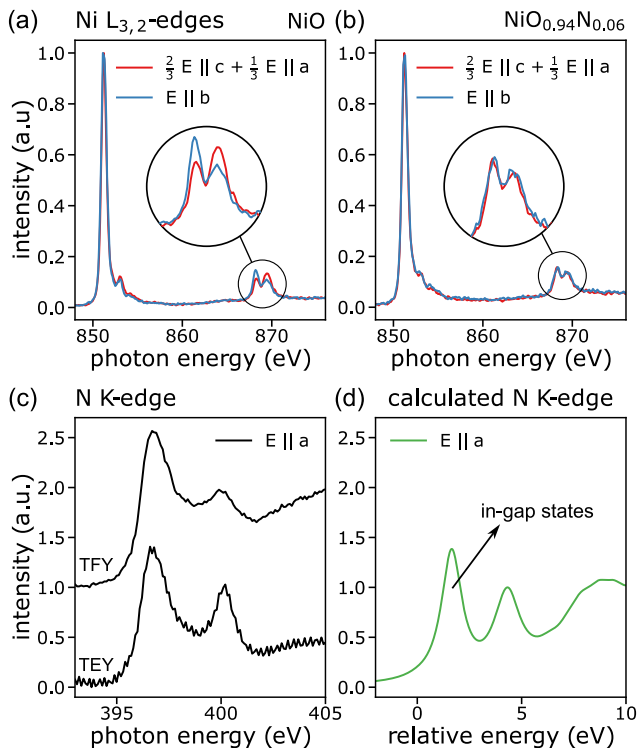


FIG. 2. X-ray absorption spectroscopy (XAS) of $\text{NiO}_{1-x}\text{N}_x$. Ni $L_{3,2}$ -edges of (a) NiO and (b) $\text{NiO}_{0.94}\text{N}_{0.06}$, at grazing incidence. The change in dichroism implies that the magnetic order is affected upon substitution. The spectra are taken in IPFY mode at the O 1s emission energy. (b) Experimental N K-edge of $\text{NiO}_{0.94}\text{N}_{0.06}$ in TEY and TFY modes, at normal incidence. The first peak arises from the in-gap states. (d) Calculated N K-edge from the DFT results. A 1 eV Lorentzian broadening is applied to replicate the experimental results.

the Ni 3d e_g electrons leads to a net spin moment $S = 1$ at each Ni site, as dictated by Hund’s rules. Replacing one O by N introduces an extra spin $S = 1/2$ due to the absence of a 2p electron. This hole dominates the superexchange interaction, and the N spin now has an AFM exchange interaction with either of the nearest-neighbor Ni atoms.

For instance, a $2p_z$ -oriented N orbital will couple exclusively with the $3d_{3z^2-r^2}$ orbitals of the Ni cations. We can estimate the hopping integral $t_{pd} \approx 1.5$ eV between $2p_z$ and $3d_{3z^2-r^2}$. Considering the charge-transfer energy $\Delta \approx 4$ eV [Fig. 1(b)] and the Coulomb interaction between the two N holes $U_{pp} \approx 3$ eV, we find:

$$J_{pd} = \frac{t_{pd}^2}{\Delta + U_{pp}} \approx 300 \text{ meV}, \quad (1)$$

with a 180° bond between the N and each Ni. This Ni-N AFM interaction dominates the superexchange interaction and, in turn, leads to a FM spin orientation between the two Ni via double exchange.

As previously mentioned, this results in a spin config-

uration with two degenerate states: $(\uparrow\uparrow - \downarrow - \uparrow\uparrow)$ and $(\downarrow\downarrow - \uparrow - \downarrow\downarrow)$. This degeneracy suggests that the Ni-N-Ni unit is completely decoupled from the rest of the lattice, meaning it is now necessary to take into account the quantum fluctuations of this system. The Hund’s rule coupling $J_H \approx 1$ eV[17], which gives rise to the spin-1 state of Ni, is significantly larger than J_{pd} , resulting in a total spin ground state of $S = 3/2$. The value of J_{pd} we find here is larger than the one resulting from the DFT calculations ($J_{pd} \approx 150$ meV). This difference arises due to DFT underestimating the exchange interaction between specific orbitals,

Overall, since the AFM lattice does not provide a net field on the Ni-N-Ni unit, the 4 Zeeman states ($m_s = -3/2, -1/2, 1/2, 3/2$) are degenerate. Similarly to quantum sensors[18], a local external magnetic field \mathbf{B}_{ext} would lead to Zeeman splitting and lift the degeneracy.

We study these effects experimentally in $\text{NiO}_{1-x}\text{N}_x$ thin films grown by MBE using NO gas on MgO (001) substrates. The N-substituted NiO films retain the same rock-salt crystal structure as NiO control samples. We show in Supplementary Material[13] their high crystallinity, confirmed using reflection high-energy electron diffraction (RHEED) and high-resolution X-ray diffraction (HRXRD), and discuss the growth details.

We present here XAS measurements, focusing our attention on $\text{NiO}_{0.94}\text{N}_{0.06}$, which allows for both diluted N concentration and high signal intensity. The XAS results for the unsubstituted and substituted samples at room temperature are presented in Fig. 2. The Ni $L_{3,2}$ -edges in NiO are resolved using inverse partial fluorescence yield (IPFY) [see Fig. 2(a)]. Linear dichroism in the L_2 absorption edge of NiO arises from the long-range AFM order and local crystal field effects[19–21]. The impact of the AFM order on the dichroism intensity is dominant in thick epitaxial films, as the ones studied here[22]. The orientation of the spin components is influenced by the strain in the films. The larger lattice parameter of MgO compared to NiO leads to tensile strain of $\approx 0.85\%$, which aligns them out-of-plane with respect to the (001) surface. It is also possible to align the spins in-plane through compressive strain, for example using Ag (001) substrates[23]. The dichroism in Fig. 2(a), observed at a grazing angle of $\theta = 30^\circ$, confirms the out-of-plane spin component in our NiO samples. Figure 2(b) shows that this dichroism is suppressed completely upon N substitution. This supports the presence of a spin-flipped Ni for each N [see Fig. 1(a)], which would hinder the signal of the dichroism.

The N K-edge spectra of a 6% substituted sample taken in total electron yield (TEY) and total fluorescence yield (TFY) modes at normal incidence are shown in Fig. 2(c). We observe a prominent double peak located at 396.7 and 400.1 eV. A similar feature is also found in various nickel nitrides[24–26]. We confirm the origin of these features by calculating the absorption spectra from DFT.

Figure 2(d) shows the calculated spectra, which align well with the experimental results under a 1 eV Lorentzian broadening. We show in Supplementary Material[13] the raw data along with the contribution of the $2p_z$, $2p_y$, and $2p_x$ orbitals. The available impurity states of N character, seen ~ 1.8 eV above the Fermi energy in Fig. 1(d), are probed directly and form the first peak. The 2nd peak corresponds to hybridized N 2p and Ni 3d states in the conduction band. The in-gap states are also seen experimentally at the O K-edge as a shoulder to the pre-edge, increasing in intensity as a function of N concentration [see Supplementary Material [13]]. The comparable N K-edge spectra observed in both TEY and TFY modes indicate a similar behavior between the surface layers and the bulk.

To reveal the band structures, we use *ex situ* ARPES measurements to probe the valence band of N-substituted NiO. Such studies in unsubstituted NiO itself are limited due to the charging issue[27, 28].

The ground state of NiO is influenced by the hybridization between Ni 3d and O 2p, and can be expressed as $\alpha|3d^8\rangle + \beta|3d^9\underline{L}\rangle + \gamma|3d^{10}\underline{L}^2\rangle$ [29]. \underline{L} denotes a ligand hole from the electron donation of O to Ni. This results in a complex spectrum spanning from 0 to -8 eV. We show in Supplementary Material[13] our ability to observe clear constant-energy maps, which further confirms the high crystallinity and resilience to air exposure of the substituted samples. The scans are taken at 85 eV and grazing incidence ($\theta = 25^\circ$). Figure 3(a) shows the cuts along Γ to X of $\text{NiO}_{0.94}\text{N}_{0.06}$. The high-intensity Ni 3d band is seen at -2.2 eV, while the hybridized states of O 2p and Ni 3d characters spread down to -8 eV.

The N 2p states introduced at the top of the valence create a new band around -0.75 eV, in agreement with the DFT calculations in Fig. 1(d). We resolve this band in Figure 3(b) by looking at the 2nd derivative of the Γ -X cut with a logarithmic scale in intensity in a 12% substituted sample. This band shows limited dispersion and a larger weight around Γ and X. The emergence of this feature from 6 to 12% substitution is seen clearly in Fig. 3(c) as a shoulder in the angle-integrated valence band. Both spectra show a peak separation of ~ 1.5 eV between the energy at the highest intensity of the valence band and its shoulder. The intensity ratio of these states from 6 to 12% substitution is 2 ± 0.4 .

The N 1s XPS measurement shown in Fig. 4 allows us to confirm the nature of the hole in N-substituted NiO. The spectrum shows a double peak contribution similar to other oxynitrides[30]. In $\text{NiO}_{0.94}\text{N}_{0.06}$, we find a peak separation of 1.5 ± 0.1 eV and an intensity ratio of 2.8 ± 0.3 eV, consistent with the expected triplet to singlet 3:1 ratio. This points to a coupling between the N 2p electrons and the core hole (a single peak would be observed otherwise) and confirms the N 2p nature of the introduced holes. We calculate all the N concentrations in this manuscript by comparing the intensity ratios and

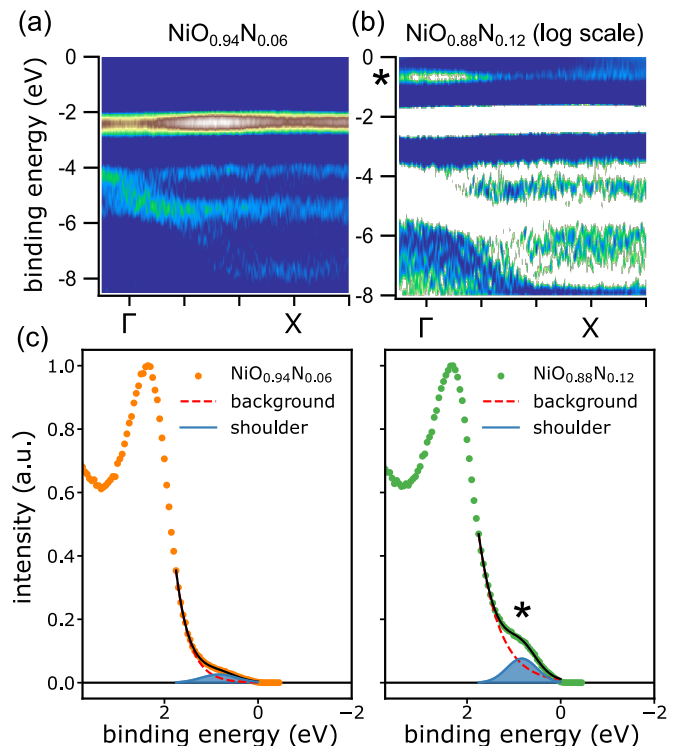


FIG. 3. Angle-resolved photoemission spectroscopy (ARPES) of $\text{NiO}_{1-x}\text{N}_x$ with incoming photon energy of 85 eV. (a) Momentum distribution curve (MDC) 2nd derivative of Γ -X cuts in $\text{NiO}_{0.94}\text{N}_{0.06}$. (b) MDC 2nd derivative in logarithmic scale of Γ -X cuts in $\text{NiO}_{0.88}\text{N}_{0.12}$. The N 2p shoulder emerges around Γ and X, and shows minimal dispersion. (c) Comparison of the normalized valence band of 6 and 12% N-substituted NiO. The shoulder at the top of the valence band arises from the N 2p states and shows a 1:2 intensity ratio between 6 and 12%.

atomic sensitivity factors of N 1s and Ni 2p[31], and show additional XPS data in Supplementary Material[13].

The combined results of the spectroscopy measurements presented in this letter complete our understanding of the $\text{NiO}_{1-x}\text{N}_x$ system and corroborate the properties predicted by our DFT calculations. These calculations demonstrate that the presence of an N leads to the formation of Ni-N-Ni units, which are decoupled from the AFM lattice and exhibit degenerate states. We observe that the suppressed dichroism at the Ni L_2 -edge supports this lowest energy configuration in DFT. By comparing the experimental and calculated N K-edge XAS, we confirm the in-gap impurity states of N 2p hole character predicted by DFT. The additional states above the valence band result in an emerging band in ARPES, with their intensity scaling linearly with respect to N substitution. The hole character of the introduced N states is identified in the N 1s XPS.

In conclusion, we conducted a comprehensive study of N substitution in NiO and re-examined its ground state in comparison to its unsubstituted stoichiometric coun-

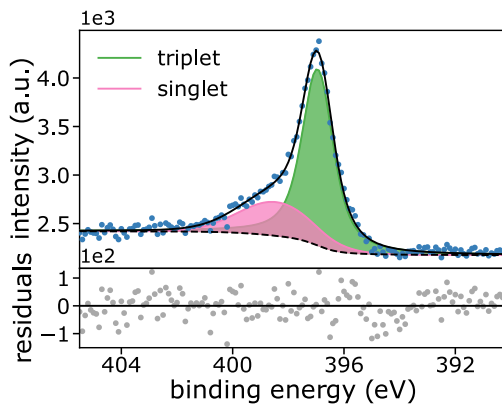


FIG. 4. N 1s X-ray photoelectron spectroscopy (XPS) of $\text{NiO}_{1-x}\text{N}_x$ with incoming photon energy of 1486.7 eV (Al K-alpha). The triplet to singlet ratio is 2.9 ± 0.3 . The peaks and backgrounds are fitted simultaneously using the SVSC background (peak Shirley)[32].

terpart. The intriguing physics observed by introducing individual N atoms into NiO opens new possibilities for designing individual defect centers in strongly correlated, AFM insulators. Since local external magnetic fields can lift the degeneracy of the Ni-N-Ni unit, this advancement could guide the development of future quantum sensors. Additionally, at finite temperatures, thermally excited magnons in the AFM lattice will cause local fluctuations in the spin environment near the Ni-N-Ni units. These fluctuations could mediate an effective, short-range coupling between two nearby units. This coupling might lift the degeneracy of the Zeeman states, with the strength of the effect determined by the proximity of the units and the temperature-dependent effective range of the fluctuations. The ability to control such electronic and magnetic properties at the atomic level underscores a potential for novel quantum devices and other advanced technological applications. Another promising direction for future research is to extend N substitution to perovskites and infinite-layer nickelates. Such studies remain scarce[33], and the effects of anion substitution on superconductivity are not yet understood. Exploring this uncharted territory could yield significant insights into the fundamental physics of these materials and their potential applications in quantum technology.

Acknowledgement—This research was undertaken thanks in part to funding from the Max Planck-UBC-UTokyo Center for Quantum Materials and the Canada First Research Excellence Fund, Quantum Materials and Future Technologies Program. The work at the University of British Columbia was also supported by the Canada Foundation for Innovation (CFI) and the British Columbia Knowledge Development Fund (BCKDF). Part of the research described in this paper was performed at the Canadian Light Source, a national research fa-

cility of the University of Saskatchewan, which is supported by the Canada Foundation for Innovation (CFI), the Natural Sciences and Engineering Research Council (NSERC), the Canadian Institutes of Health Research (CIHR), the Government of Saskatchewan, and the University of Saskatchewan. This research used resources of the Advanced Light Source, which is a DOE Office of Science User Facility under contract no. DE-AC02-05CH11231.

* Corresponding author: sgodin@phas.ubc.ca

- [1] J. Zaanen, G. A. Sawatzky, and J. W. Allen, Band gaps and electronic structure of transition-metal compounds, *Physical Review B* **55**, 418 (1985).
- [2] N. B. Weber, H. Ohldag, H. Gomonaj, and F. U. Hillebrecht, Magnetostrictive domain walls in antiferromagnetic nio, *Physical Review Letters* **91**, 237205 (2003).
- [3] K. Arai, T. Okuda, A. Tanaka, M. Kotsugi, K. Fukumoto, T. Ohkochi, T. Nakamura, T. Matsushita, T. Muro, M. Oura, Y. Senba, H. Ohashi, A. Kakizaki, C. Mitsumata, and T. Kinoshita, Three-dimensional spin orientation in antiferromagnetic domain walls of nio studied by x-ray magnetic linear dichroism photoemission electron microscopy, *Physical Review B* **85**, 104418 (2012).
- [4] S. Park, K. Jin, H. K. Lim, J. Kim, K. H. Cho, S. Choi, H. Seo, M. Y. Lee, Y. H. Lee, S. Yoon, M. Kim, H. Kim, S. H. Kim, and K. T. Nam, Spectroscopic capture of a low-spin mn(iv)-oxo species in ni-mn3o4 nanoparticles during water oxidation catalysis, *Nature Communications* **11**, 1 (2020).
- [5] T. V. Thi, A. K. Rai, J. Gim, and J. Kim, High performance of co-doped nio nanoparticle anode material for rechargeable lithium ion batteries, *Journal of Power Sources* **292**, 23 (2015).
- [6] J. M. Taylor, P. Cappellaro, L. Childress, L. Jiang, D. Budker, P. R. Hemmer, A. Yacoby, R. Walsworth, and M. D. Lukin, High-sensitivity diamond magnetometer with nanoscale resolution, *Nature Physics* **4**, 810 (2008).
- [7] K. O. Ho, Y. Shen, Y. Y. Pang, W. K. Leung, N. Zhao, and S. Yang, Diamond quantum sensors: from physics to applications on condensed matter research, *Functional Diamond* **1**, 160 (2021).
- [8] J. R. Weber, W. F. Koehl, J. B. Varley, A. Janotti, B. B. Buckley, C. G. V. de Walle, and D. D. Awschalom, Quantum computing with defects, *Proceedings of the National Academy of Sciences* **107**, 8513 (2010).
- [9] D. B. Higginbottom, A. T. K. Kurkjian, C. Chartrand, M. Kazemi, N. A. Brunelle, E. R. MacQuarrie, J. R. Klein, N. R. Lee-Hone, J. Stacho, M. Ruether, C. Bowness, L. Bergeron, A. DeAbreu, S. R. Harrigan, J. Kanaganayagam, D. W. Marsden, T. S. Richards, L. A. Stott, S. Roorda, K. J. Morse, M. L. W. Thewalt, and S. Simmons, Optical observation of single spins in silicon, *Nature* **607**, 266 (2022).
- [10] L. Bergeron, C. Chartrand, A. T. Kurkjian, K. J. Morse, H. Riemann, N. V. Abrosimov, P. Becker, H. J. Pohl, M. L. Thewalt, and S. Simmons, Silicon-integrated telecommunications photon-spin interface, *PRX Quantum*

- tum **1**, 1 (2020).
- [11] H. L. Stern, C. M. Gilardoni, Q. Gu, S. E. Barker, O. F. J. Powell, X. Deng, S. A. Fraser, L. Follet, C. Li, A. J. Ramsay, H. H. Tan, I. Aharonovich, and M. Atatüre, A quantum coherent spin in hexagonal boron nitride at ambient conditions, *Nature Materials* **23**, 1379 (2024).
- [12] G. Wolfowicz, C. P. Anderson, B. Diler, O. G. Poluektov, F. J. Heremans, and D. D. Awschalom, Vanadium spin qubits as telecom quantum emitters in silicon carbide, *Science Advances* **6**, 2 (2020).
- [13] See Supplementary Material for details of the thin film fabrication and additional DFT, XAS, ARPES and XPS results.
- [14] C. de Graaf, R. Broer, and W. Nieuwpoort, Comparison of the superexchange interaction in nio and in a nio[100] surface, *Chemical Physics Letters* **271**, 372 (1997).
- [15] T. Chatterji, G. J. McIntyre, and P.-A. Lindgard, Antiferromagnetic phase transition and spin correlations in nio, *Physical Review B* **79**, 172403 (2009).
- [16] M. T. Hutchings and E. J. Samuelsen, Measurement of spin-wave dispersion in nio by inelastic neutron scattering and its relation to magnetic properties, *Physical Review B* **6**, 3447 (1972).
- [17] K. Terakura, T. Oguchi, A. R. Williams, and J. Kübler, Band theory of insulating transition-metal monoxides: Band-structure calculations, *Physical Review B* **30**, 4734 (1984).
- [18] S. Zhang, K. Bian, and Y. Jiang, Perspective: nanoscale electric sensing and imaging based on quantum sensors, *Quantum Frontiers* **2**, 19 (2023).
- [19] D. Alders, L. H. Tjeng, F. C. Voogt, T. Hibma, G. A. Sawatzky, C. T. Chen, J. Vogel, M. Sacchi, and S. Iacobucci, Temperature and thickness dependence of magnetic moments in nio epitaxial films, *Physical Review B* **57**, 11623 (1998).
- [20] S. Krishnakumar, M. Liberati, C. Grazioli, M. Veronese, S. Turchini, P. Luches, S. Valeri, and C. Carbone, Magnetic linear dichroism studies of in situ grown nio thin films, *Journal of Magnetism and Magnetic Materials* **310**, 8 (2007).
- [21] F. de Groot, Differences between l3 and l2 x-ray absorption spectra, *Physica B: Condensed Matter* **208-209**, 15 (1995).
- [22] M. W. Haverkort, S. I. Csiszar, Z. Hu, S. Altieri, A. Tanaka, H. H. Hsieh, H.-J. Lin, C. T. Chen, T. Hibma, and L. H. Tjeng, Magnetic versus crystal-field linear dichroism in nio thin films, *Physical Review B* **69**, 020408 (2004).
- [23] S. Altieri, M. Finazzi, H. H. Hsieh, H. J. Lin, C. T. Chen, T. Hibma, S. Valeri, and G. A. Sawatzky, Magnetic dichroism and spin structure of antiferromagnetic nio(001) films, *Physical Review Letters* **91**, 137201 (2003).
- [24] N. Pandey, M. Gupta, and J. Stahn, Study of reactively sputtered nickel nitride thin films, *Journal of Alloys and Compounds* **851**, 156299 (2021).
- [25] B. You, X. Liu, G. Hu, S. Gul, J. Yano, D. en Jiang, and Y. Sun, Universal surface engineering of transition metals for superior electrocatalytic hydrogen evolution in neutral water, *Journal of the American Chemical Society* **139**, 12283 (2017).
- [26] H. Jin, X. Liu, S. Chen, A. Vasileff, L. Li, Y. Jiao, L. Song, Y. Zheng, and S.-Z. Qiao, Heteroatom-doped transition metal electrocatalysts for hydrogen evolution reaction, *ACS Energy Letters* **4**, 805 (2019).
- [27] K. Gillmeister, D. Golež, C.-T. Chiang, N. Bittner, Y. Pavlyukh, J. Berakdar, P. Werner, and W. Widdra, Ultrafast coupled charge and spin dynamics in strongly correlated nio, *Nature Communications* **11**, 4095 (2020).
- [28] Z.-X. Shen, R. S. List, D. S. Dessau, B. O. Wells, O. Jepsen, A. J. Arko, R. Bartlett, C. K. Shih, F. Parmigiani, J. C. Huang, and P. A. P. Lindberg, Electronic structure of nio: Correlation and band effects, *Physical Review B* **44**, 3604 (1991).
- [29] M. A. van Veenendaal and G. A. Sawatzky, Nonlocal screening effects in 2 p x-ray photoemission spectroscopy core-level line shapes of transition metal compounds, *Physical Review Letters* **70**, 2459 (1993).
- [30] I. S. Elfimov, A. Rusydi, S. I. Csiszar, Z. Hu, H. H. Hsieh, H.-J. Lin, C. T. Chen, R. Liang, and G. A. Sawatzky, Magnetizing oxides by substituting nitrogen for oxygen, *Physical Review Letters* **98**, 137202 (2007).
- [31] J. F. Moulder, W. F. Stickle, P. E. Sobol, and K. D. Bomben, *Handbook of X-ray Photoelectron Spectroscopy* (Physical Electronics, Inc., 1995) pp. 1-261.
- [32] A. Herrera-Gomez, M. Bravo-Sanchez, O. Ceballos-Sanchez, and M. O. Vazquez-Lepe, Practical methods for background subtraction in photoemission spectra, *Surface and Interface Analysis* **46**, 897 (2014).
- [33] C. Yang, Y. Tian, C. Yang, G. Kim, J. Pu, and B. Chi, Recent progress and future prospects of anions o-site doped perovskite oxides in electrocatalysis for various electrochemical systems, *Advanced Science* **10**, 1 (2023).

Supplementary Material for: Novel Magnetic Ni-N-Ni Centers in N-substituted NiO

Simon Godin,^{1,2,*} Ilya S. Elfimov,^{1,2} Fengmiao Li,^{1,2} Bruce A. Davidson,^{1,2} Ronny Sutarto,³ Jonathan D. Denlinger,⁴ Liu Hao Tjeng,⁵ George A. Sawatzky,^{1,2} and Ke Zou^{1,2}

¹Department of Physics and Astronomy, University of British Columbia, Vancouver, British Columbia V6T 1Z4, Canada

²Quantum Matter Institute, University of British Columbia, Vancouver, British Columbia V6T 1Z4, Canada

³Canadian Light Source, Saskatoon, Saskatchewan S7N 2V3, Canada

⁴Advanced Light Source, Lawrence Berkeley National Laboratory, Berkeley, CA 94720, USA

⁵Max Planck Institute for Chemical Physics of Solids, Nöthnitzer Straße 40, 01187 Dresden, Germany

(Dated: December 31, 2024)

THIN FILM FABRICATION

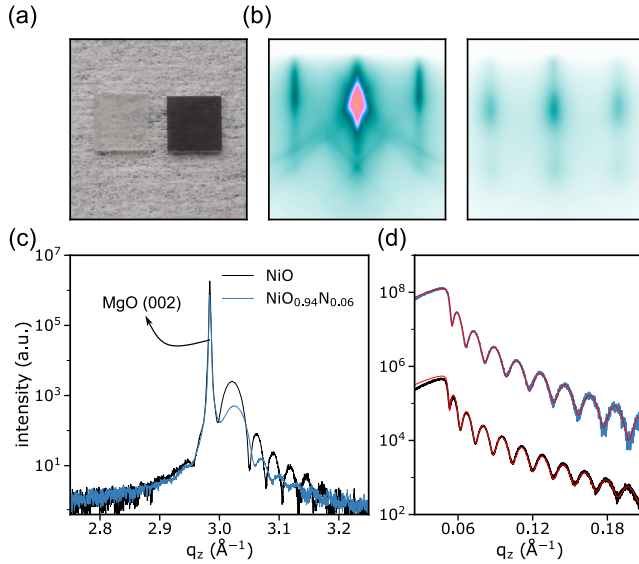


FIG. 1. Structure and crystal quality of NiO and $\text{NiO}_{0.94}\text{N}_{0.06}$. (a) Picture of NiO and $\text{NiO}_{0.94}\text{N}_{0.06}$ samples. (b) RHEED images of NiO (001) and $\text{NiO}_{0.94}\text{N}_{0.06}$ (001) in the [100] direction. (c) XRD spectra of NiO and $\text{NiO}_{0.94}\text{N}_{0.06}$, showing thickness fringes for both films. Note the decreased lattice parameter upon N substitution. The scans are shifted to match the baseline of both backgrounds. (d) XRR spectra of NiO and $\text{NiO}_{0.94}\text{N}_{0.06}$. The simulations in red show a thickness of 347 ± 1 and 297.0 ± 0.7 \AA , respectively.

In this Section, we describe the growth and characterization of NiO and N-substituted NiO. N-substituted NiO films have previously been synthesized using deposition techniques, such as radio-frequency magnetron sputtering in N_2 environment[1, 2], or spray pyrolysis[3]. These techniques generate polycrystalline or amorphous films. However, single-crystalline synthesis of substituted films is desirable for complete characterization and necessary to limit undesired defects and disorder. We instead use nitrogen oxide (NO) gas-assisted molecular beam epitaxy (MBE), which allows us to have fine control over the substitution concentration and high crystallinity. As in other compounds[4, 5], the inclusion of N is achieved by lower-

ing the NO gas pressure and the substrate temperature during growth. This would normally lead to O deficiency in the system, but here allows for the substitution of the O sites by N instead.

The films presented in the main text are grown epitaxially on MgO (001). We use MgO as a substrate due to its rock-salt structure and the $< 1\%$ lattice mismatch from NiO [6]. The substrates are cleaned with ethanol and methanol and annealed in ultra-high vacuum (UHV) at 800°C . In our apparatus, the NO gas is carried from a leak valve by a feedthrough directed at the sample's surface to raise the effective flux. This method allows good control over the N substitution level by varying the growth temperature and NO gas pressure. The films presented here are grown at 150°C and NO pressure ranging from 1×10^{-6} to 4×10^{-7} Torr. This results in N atom concentrations ranging from 6 to 12%. The unsubstituted NiO control sample is grown at 500°C in molecular O pressure of 5×10^{-6} Torr. We compare exemplary unsubstituted NiO and 6% substituted $\text{NiO}_{1-x}\text{N}_x$ films in Fig. 1. We see from Fig. 1(a) that the films become darker with substitution. This effect, along with the increased conductivity of the samples, provides a useful way to quickly confirm the presence of N.

Reflection high-energy electron diffraction (RHEED) measurements confirm the same rock-salt structure of $\text{NiO}_{1-x}\text{N}_x$ as NiO [Fig. 1(b)]. The substituted films carry different features in RHEED, i.e. modulated streaks. This indicates higher surface roughness, although the strong streak intensity implies the single orientation and good quality of the films at the surface. High-resolution X-ray diffraction scans (HRXRD) show high crystallinity in the bulk of both samples [Fig. 1(c)], indicated by the presence of thickness fringes. Both $\text{NiO}_{1-x}\text{N}_x$ and NiO have tensile strain on the MgO substrate, leading to a smaller lattice parameter in the c direction and a tetragonal unit cell, due to the biaxial strain. N substitution also slightly reduces the c lattice parameter. The XRR scans in Fig. 1(d) show clear oscillations for both films. The thickness of the samples, ranging from 30 to 35 nm, is determined by simulation of the XRR spectra using the GenX software[7].

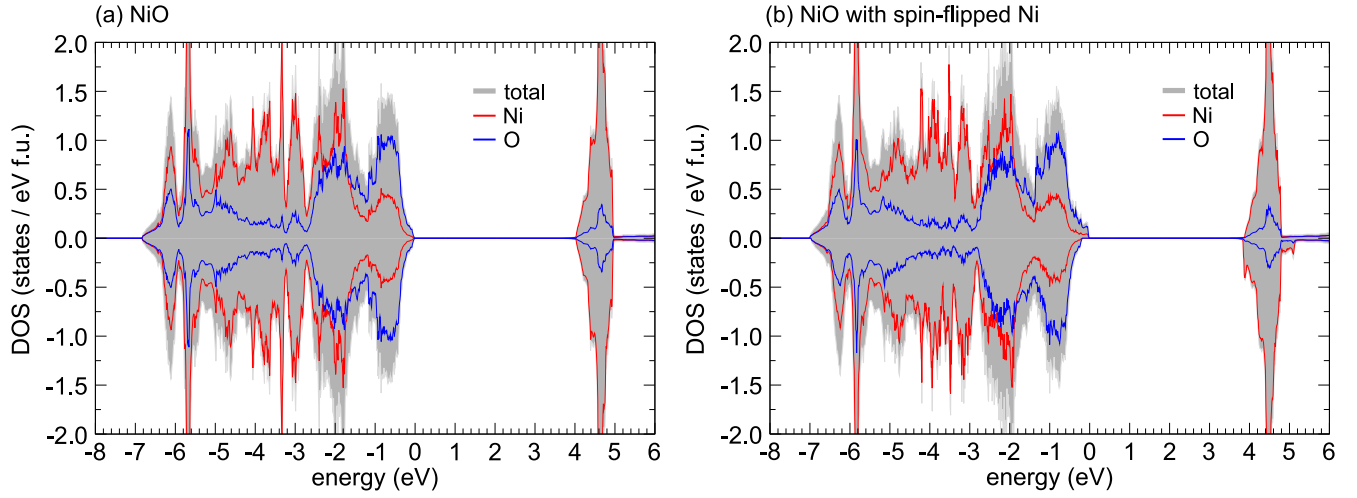


FIG. 2. Additional DFT calculations for different configurations in an unsubstituted NiO unit cell with 32 anion and cation sites. PDoS of (a) NiO and (b) NiO with one spin-flipped Ni. The cost to flip the magnetic moment of the Ni is 117 meV. The conductivity gap is reduced to 3.44 eV from 3.63 eV between both configurations. The zero of energy is at the Fermi energy.

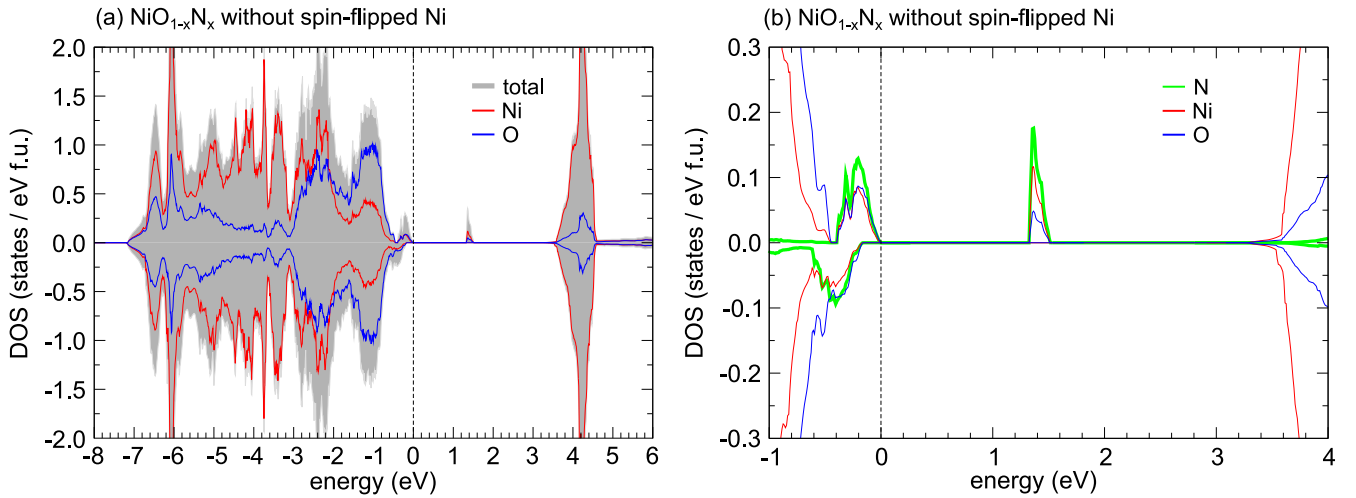


FIG. 3. Additional DFT calculations for different configurations in an N-substituted NiO unit cell with 32 anion and cation sites. (a) PDoS of $\text{NiO}_{1-x}\text{N}_x$ with one O substituted for N, but without the spin-flipped Ni configuration. This solution raises the energy of the system by 204 meV. (b) Zoom of (a) around the bandgap, showing the N states. The N states are not shown in (b). The zero of energy is at the Fermi energy.

DFT CALCULATIONS AND ADDITIONAL CONFIGURATIONS

The spin-polarized DFT calculations for spin-flipped $\text{NiO}_{1-x}\text{N}_x$ in the main text are performed with the Quantum Espresso code[8, 9], using the projector augmented wave (PAW) method[10]. The Perdew-Burke-Ernzerhof (PBE) functional[11] is used for the exchange-correlation energy. The kinetic energy cutoff for wavefunctions is 1088.5 eV. The Brillouin zone of $2 \times 2 \times 2$ supercell is sampled using $8 \times 8 \times 8$ k-grid. The Dudarev et al. formulation of DFT+U method[12, 13] is used throughout with Ni 3d, O 2p and N 2p electrons' on-site effective interactions $U = 6$ eV, 4 eV, and 3 eV, respectively. The calculated bulk NiO lattice constant of 4.24 Å and the band gap of 3.63 eV are in good agreement with experimental observations. N XAS spectra are calculated using the theoretical approach after Gougoussis et al.[14, 15].

Additional PDoS from DFT calculations are shown in Fig. 2 and Fig. 3. The energy cost of flipping a Ni spin in unsubstituted NiO is 117 meV [Fig. 2(a) and Fig. 2(b)]. On the other hand, the arrangement with no Ni spin-flip in $\text{NiO}_{1-x}\text{N}_x$ [Fig. 3(a) and Fig. 3(b)] raises the ground state energy by 204 meV compared to the one in the main text. While the N atom in the Ni spin-flipped configuration stays in the center of the Ni octahedral, this is not the case for this high-energy state. The N atom moves along the (111) plane, resulting in Ni-N interatomic distances of 4.361 Å in the z direction and 4.207 Å in the x and y direction. Figure 4 shows the spin-density map of this system. It allows for easy visualization of the N hole and spin-flipped Ni pair, with the N orientated towards the Ni. This changes the AFM Ni-O-Ni into Ni-N-Ni with both Ni spins in the same direction, opposite to the spin of the N hole.

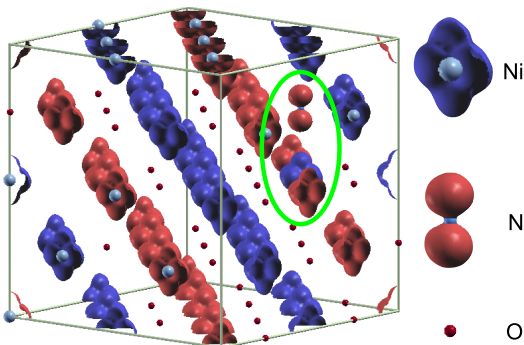


FIG. 4. (c) Spin density showing the orientation of N spin density with respect to Ni site whose magnetic moment is changed with respect to bulk NiO AFM structure. Spin-up and spin-down states are indicated in blue and red, respectively.

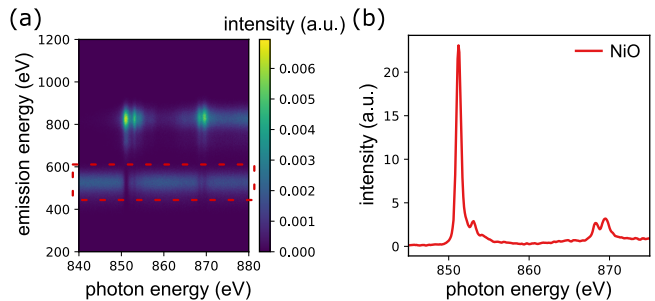


FIG. 5. XAS IPFY spectrum of the Ni $L_{3,2}$ -edges in NiO. (a) Photon vs. emission energy map. The Ni $L_{3,2}$ -edges (850-870 eV) show self-absorption effects. The O 1s contribution (530-580 eV) in the red dashed rectangle are summed over and inverted to obtain the IPFY data (b).

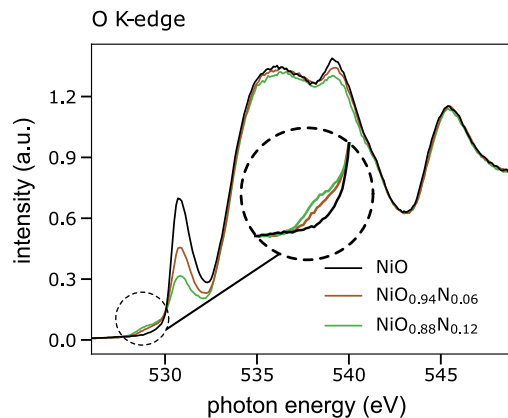


FIG. 6. XAS of $\text{NiO}_{1-x}\text{N}_x$ at the O K-edge in TFY mode as a function of substitution, which suppresses the pre-edge and introduces a shoulder (blown-up region).

XAS AND CALCULATED N K-EDGE

The XAS measurements in the main text are conducted under linear polarized light. At normal incidence ($\theta = 90^\circ$), the polarization vectors are along $E \parallel a$ and $E \parallel b$. Grazing incidence ($\theta = 30^\circ$) leads to $(2/3 E \parallel c + 1/3 E \parallel a)$ and $E \parallel b$. This geometry is shown in Fig. 7(b). We use three modes of detection, namely total fluorescence and electron yield (TFY and TEY), as well as inverse partial fluorescence yield (IPFY)[16]. Each mode comes with its own set of advantages and is used in this paper.

The TEY mode offers a shallower penetration depth and a spectrum closer to the actual absorption coefficient compared to the TFY mode. This is due to the self-absorption effects that populate the fluorescence yield, originating from additional absorption at the edge's resonant energies. However, the TEY mode typically suffers from significant charging effects due to the insulating nature of NiO. This makes it particularly difficult to compare the substituted films to unsubstituted NiO

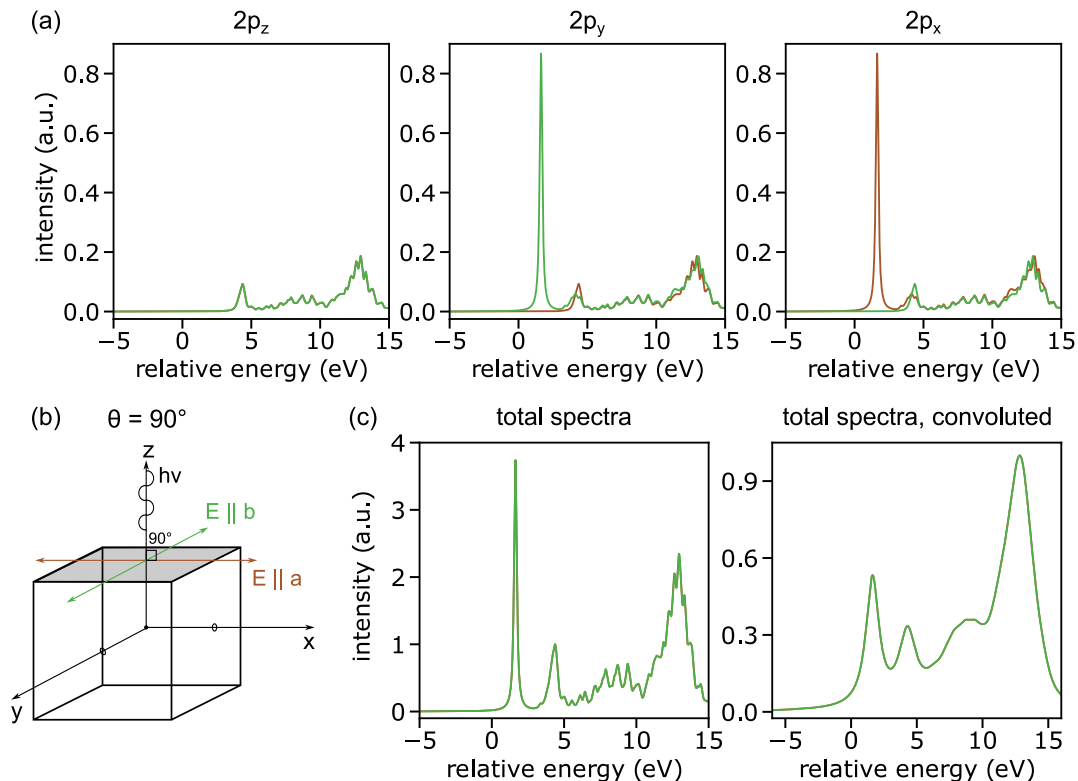


FIG. 7. Calculated XAS N K-edge from the DFT results in the main text. (a) Calculated N K-edge, resolved for p_z , p_y and p_x . (b) Geometry of the polarization of the incoming light at normal incidence. The shaded area shows the surface of the sample. (c) Total spectra, with and without a 1 eV Lorentzian broadening.

since they have a large difference in resistivity. Lastly, the IPFY mode resolves outgoing photon energy and uses the contribution of a non-resonant transition at lower detected energy to extract the spectra without including charging or self-absorption effects. With this in mind, we choose to analyze the O K-edge using TFY, since we compared $\text{NiO}_{1-x}\text{N}_x$ and NiO. The use of both TEY and TFY for the N K-edge is ideal due to the limited difference in charging effects between different substitution levels, as well as allowing the comparison of different probing depths. For the Ni $L_{3,2}$ -edges, the high intensity of the O 1s states at lower emission energy allows for the use of IPFY, as shown in Fig. 5. This leads to spectra that are the closest to the absorption coefficient.

The process to obtain the IPFY XAS spectrum of the Ni $L_{3,2}$ -edges in NiO is shown in Fig. 5. The photon vs. emission energy map in Fig. 5(a) contains both the Ni 2p and O 1s states, around 850 and 550 eV, respectively. The intensity near Ni 2p includes self-absorption effects, while the dip in intensity near O 1s reflects the absorption coefficient without such effects. The resulting Ni $L_{3,2}$ -edges absorption is seen in Fig. 5(b), by taking the inverse of the O 1s states in the red dashed rectangle in (a).

The TFY spectra at the O K-edge for 0, 6, and 12% substituted films are shown in Fig. 6. A pre-edge is

present at 530.5 eV, due to hybridization between Ni 3d and O 2p states. The reduction in the pre-edge intensity as a function of substitution shows a larger ratio than 6 and 12%. This can be understood by the fact that each N has 6 Ni nearest-neighbors, affecting their hybridization with O significantly. A new peak also emerges at 529 eV, emphasized by the dashed circle, originating from the N 2p states introduced in the bandgap. The intensity is higher with increasing N doping levels.

Figure 7(a) shows the calculated XAS spectra for the 1s to 2p transitions of the N K-edge, resolved for $2p_z$, $2p_y$ and $2p_x$. The geometry of the experimental and calculated N K-edge are identical. Note that at normal incidence, the $2p_y$ and $2p_x$ spectra are identical, but with reversed polarization, as expected from a cubic system. Figure 7(c) shows the resulting total spectra. A 1 eV Lorentzian broadening leads to good agreement with the experimental data.

ARPES AND XPS ANALYSIS

We present here additional ARPES and XPS results for $\text{NiO}_{1-x}\text{N}_x$. Fig. 8(a) shows constant-energy maps of $\text{NiO}_{0.88}\text{N}_{0.12}$ at a binding energy of -4 eV (crossing of the hybridized O 2p and Ni 3d bands) and -1 eV (N 2p

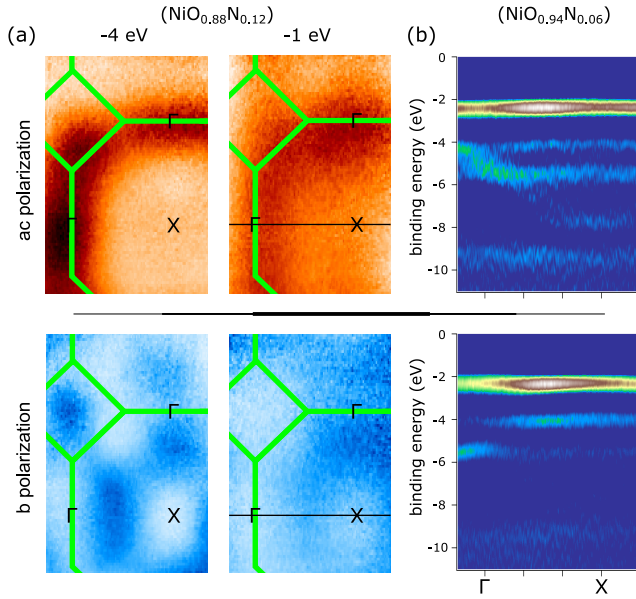


FIG. 8. ARPES on $\text{NiO}_{1-x}\text{N}_x$ with incoming photon energy of 85 eV and grazing incidence ($\theta = 25^\circ$). (a) Constant-energy maps at binding energies of -4 and -1 eV with ac and b polarizations. The 12% substituted sample is shown to resolve the N states at -1 eV. (b) Momentum Distribution Curve (MDC) 2^{nd} derivative of Γ -X cuts in $\text{NiO}_{0.94}\text{N}_{0.06}$.

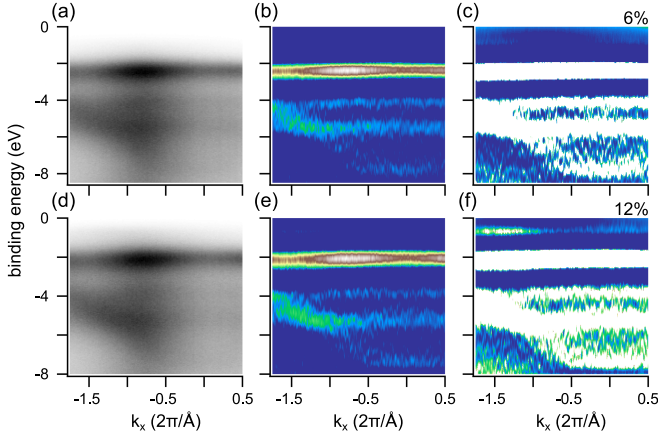


FIG. 9. Comparison of the Γ -X cuts in the ARPES spectra of 6 and 12% substituted films for raw data (a, d) and 2^{nd} derivative (b, e). Taking the logarithm scale in intensity of the 2^{nd} derivative (c, f) emphasizes the N 2p band, located around -0.75 eV.

states in the valence band). These scans are taken *ex situ*, after a simple degassing procedure at 150 °C. Our ability to observe clear constant-energy maps confirms the high crystallinity and resilience to air exposure of the substituted samples. The incoming photon energy is 85 eV and the scans are taken at grazing incidence ($\theta = 25^\circ$) in a similar geometry than XAS ($E \parallel a$ and $E \parallel b$ at normal incidence).

Figure 8(b) shows the cuts along Γ to X of

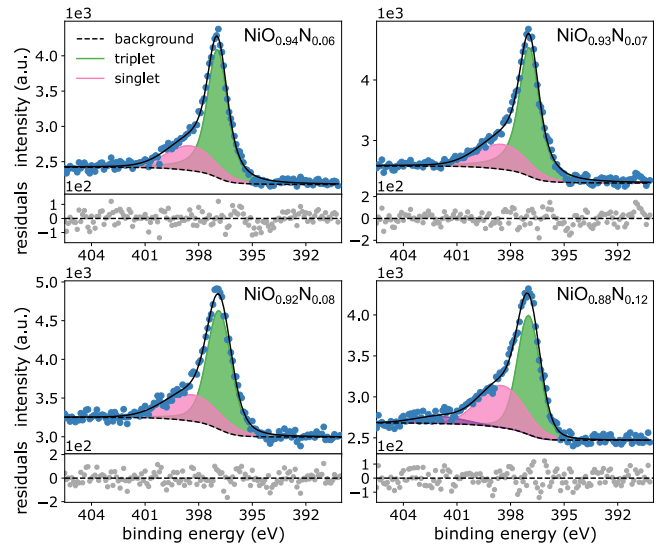


FIG. 10. XPS spectra of N 1s for 6% 7%, 8% and 12% substitution. The triplet to singlet ratios are 2.9 ± 0.3 , 2.9 ± 0.3 , 2.3 ± 0.3 and 1.5 ± 0.4 , with a χ_r^2 of 2.22, 1.48, 1.9 and 1.14 respectively. The peaks and backgrounds are fitted simultaneously using the SVSC background (peak Shirley)[17]

$\text{NiO}_{0.94}\text{N}_{0.06}$ under linear polarized light. The high-intensity Ni 3d band is seen at -2.2 eV, while the hybridized states of O 2p and Ni 3d character spread between -4 to -8 eV. A clear polarization dependence of the lowest band is observed through this whole region, indicative of out-of-plane symmetry. A core-level band is also present at -9.5 eV. Figure 9 compares the raw data [Fig. 9(a) and 9(d)] and the 2^{nd} derivative [Fig. 9(b) and Fig. 9(e)] in the case of 6% and 12% substitution. The 2^{nd} derivative is used to accurately determine the maximum intensity of the bands and reduce the background of the detector. Figure 9(c) and Fig. 9(f) show the logarithm scale of the intensity of the 2^{nd} derivative. This allows us to resolve the N 2p band for 12% substitution, located around -0.75 eV. The band is faint in the case of 6% substitution, but still visible around the Γ and X points.

Results for the XPS of the N 1s samples are shown in Fig. 10. Note that the 3:1 ratio is reduced at higher substitution. A shake-off peak also becomes visible at 12%.

* Corresponding author: sgodin@phas.ubc.ca

- [1] J. Keraudy, A. Ferrec, M. Richard-Plouet, J. Hamon, A. Goulet, and P.-Y. Jouan, Nitrogen doping on NiO by reactive magnetron sputtering: A new pathway to dynamically tune the optical and electrical properties, *Applied Surface Science* **409**, 77 (2017).
- [2] F. Lin, D. T. Gillaspie, A. C. Dillon, R. M. Richards, and C. Engrakul, Nitrogen-doped nickel oxide thin films for

- enhanced electrochromic applications, *Thin Solid Films* **527**, 26 (2013).
- [3] S. Sriram, A. Thayumanavan, and K. Ravichandran, Influence of nitrogen doping on properties of NiO films, *Surface Engineering* **32**, 207 (2016).
- [4] R. Wicks, S. G. Altendorf, C. Caspers, H. Kierspel, R. Sutarto, L. H. Tjeng, and A. Damascelli, NO-assisted molecular-beam epitaxial growth of nitrogen substituted EuO, *Applied Physics Letters* **100**, 1 (2012).
- [5] F. C. Voogt, P. J. M. Smulders, G. H. Wijnja, L. Niesen, T. Fujii, M. A. James, and T. Hibma, NO₂-assisted molecular-beam epitaxy of wustitelike and magnetitelike Fe oxynitride films on MgO(100), *Physical Review B* **63**, 125409 (2001).
- [6] S. Godin, B. A. Davidson, R. Sutarto, C. Liu, F. Li, I. S. Elfimov, G. A. Sawatzky, and K. Zou, A method to stabilize the unreconstructed MgO (111) polar surface, *Applied Physics Letters* **121**, 8 (2022).
- [7] M. Björck and G. Andersson, GenX : an extensible X-ray reflectivity refinement program utilizing differential evolution, *Journal of Applied Crystallography* **40**, 1174 (2007).
- [8] P. Giannozzi, S. Baroni, N. Bonini, M. Calandra, R. Car, C. Cavazzoni, D. Ceresoli, G. L. Chiarotti, M. Cococcioni, I. Dabo, A. D. Corso, S. de Gironcoli, S. Fabris, G. Fratesi, R. Gebauer, U. Gerstmann, C. Gougoussis, A. Kokalj, M. Lazzeri, L. Martin-Samos, N. Marzari, F. Mauri, R. Mazzarello, S. Paolini, A. Pasquarello, L. Paulatto, C. Sbraccia, S. Scandolo, G. Sclauzero, A. P. Seitsonen, A. Smogunov, P. Umari, and R. M. Wentzcovitch, QUANTUM ESPRESSO: a modular and open-source software project for quantum simulations of materials, *Journal of Physics: Condensed Matter* **21**, 395502 (19pp) (2009).
- [9] P. Giannozzi, O. Andreussi, T. Brumme, O. Bunau, M. B. Nardelli, M. Calandra, R. Car, C. Cavazzoni, D. Ceresoli, M. Cococcioni, N. Colonna, I. Carnimeo, A. D. Corso, S. de Gironcoli, P. Delugas, R. A. D. Jr, A. Ferretti, A. Floris, G. Fratesi, G. Fugallo, R. Gebauer, U. Gerstmann, F. Giustino, T. Gorni, J. Jia, M. Kawamura, H.-Y. Ko, A. Kokalj, E. Küçükbenli, M. Lazzeri, M. Marsili, N. Marzari, F. Mauri, N. L. Nguyen, H.-V. Nguyen, A. O. de-la Roza, L. Paulatto, S. Poncé, D. Rocca, R. Sabatini, B. Santra, M. Schlipf, A. P. Seitsonen, A. Smogunov, I. Timrov, T. Thonhauser, P. Umari, N. Vast, X. Wu, and S. Baroni, Advanced capabilities for materials modelling with QUANTUM ESPRESSO, *Journal of Physics: Condensed Matter* **29**, 465901 (2017).
- [10] P. E. Blochl, Projector augmented-wave method, *Phys. Rev. B* **50**, 17953 (1994).
- [11] J. P. Perdew, K. Burke, and M. Ernzerhof, Generalized Gradient Approximation Made Simple, *Phys. Rev. Lett.* **77**, 3865 (1996).
- [12] V. I. Anisimov, J. Zaanen, and O. K. Andersen, Band theory and Mott insulators: Hubbard U instead of Stoner I, *Phys. Rev. B* **44**, 943 (1991).
- [13] S. L. Dudarev, G. A. Botton, S. Y. Savrasov, C. J. Humphreys, and A. P. Sutton, Electron-energy-loss spectra and the structural stability of nickel oxide: An LSDA+U study, *Phys. Rev. B* **57**, 1505 (1998).
- [14] C. Gougoussis, M. Calandra, A. Seitsonen, C. Brouder, A. Shukla, and F. Mauri, Intrinsic charge transfer gap in NiO from Ni K-edge x-ray absorption spectroscopy, *Phys. Rev. B* **79**, 45118 (2009).
- [15] C. Gougoussis, M. Calandra, A. P. Seitsonen, and F. Mauri, First-principles calculations of x-ray absorption in a scheme based on ultrasoft pseudopotentials: From alpha-quartz to high-Tc compounds, *Phys. Rev. B* **80**, 75102 (2009).
- [16] A. J. Achkar, T. Z. Regier, E. J. Monkman, K. M. Shen, and D. G. Hawthorn, Determination of total x-ray absorption coefficient using non-resonant x-ray emission, *Scientific Reports* **1**, 182 (2011).
- [17] A. Herrera-Gomez, M. Bravo-Sanchez, O. Ceballos-Sanchez, and M. O. Vazquez-Lepe, Practical methods for background subtraction in photoemission spectra, *Surface and Interface Analysis* **46**, 897 (2014).